

layer at 1.55 bar, similar to observations of the Galileo probe<sup>7</sup>, whereas model 2 includes an additional opacity source (the water cloud) at 5.6 bars, similar to predictions from thermodynamical models<sup>1,2</sup> and some inferences from Voyager observations<sup>5</sup>. In addition, a correlated-k code including multiple scattering<sup>10</sup> was used to confirm its validity, with one cloud layer at 1.55 bar (model 3). The atmospheric thermal structure is taken from Galileo probe *in situ* measurements<sup>11</sup>. Cases were run assuming a range of RH and two models of vertical cloud structure.

Model 1 produces a good fit to hot spot spectra for an RH of less than ~1%. Model 2, which includes the 5.6-bar cloud, produces a poor fit and rules out the existence of a deep cloud within the hot spot (Fig. 2). Outside the hot spot, both models produce similarly good fits. In all cases, however, model 2 requires a much greater RH than model 1. This non-uniqueness can be understood when studying the contribution functions. They are the kernel of the radiative transfer integral, that is, the variation of the gas opacity with altitude times the emission of each atmospheric layer. When opacity varies exponentially, as in the case of an atmosphere in hydrostatic equilibrium assumed here, the contribution functions peak at a certain level, which consequently contributes most of the outgoing radiation at a given wavelength. For small values of RH, the contribution functions peak near 6 bars, so that a cloud layer at 5.6 bars strongly affects the shape of spectra measured from orbit<sup>12</sup> (Fig. 2). When RH is more than ~20%, the greatest contribution is from above the 5.6-bar level, so that the shape of the spectrum is not much affected by the presence of an opacity layer at this level. The effects of opacity at 5.6 bars are to 'cut off' contribution to the outgoing radiation from below this level, and thus require a higher water vapour concentration above this level to still fit the water band depth. Because it is not possible to unambiguously detect the presence of a water cloud in this region, the RH from model 1 should be taken as a lower limit.

Our primary finding is that extremely dry regions, such as the E4 hotspot with RH between 0.1% and 1%, exist in close proximity to humid areas, characterized by a RH of more than ~20%. The presence of a deep water cloud is excluded in the dry regions. Although the precision of derived water vapour mixing ratios is limited by model assumptions, the above analysis shows that relatively dry and humid areas are easily distinguished using the observed 5.025- $\mu\text{m}$  water band depth. Inside the hot spot the water band is shallow ( $D = 0.2\text{--}0.28$ ), whereas outside the hot spot it is generally deeper ( $D = 0.3\text{--}0.33$ ). At other locations it is very deep ( $D = 0.33\text{--}0.4$ ). Clearly, local meteorology creates a more complex distribution of relative humidity than is expected solely from thermodynamical models<sup>1,2</sup>.

Images at visible and near-infrared wavelengths from the SSI yield some insight into the local dynamics and cloud structure down to about 3 bars<sup>13</sup>. Using SSI images, deep (>3 bars) clouds have been found in the area surrounding the E4 bright cloud<sup>14</sup>. This bright cloud lies in a cyclonic shear zone, where the horizontal zonal flow is changing direction from about 100  $\text{ms}^{-1}$  eastward at 6° N to about 25  $\text{ms}^{-1}$  westward at 15° N (ref. 15). Cyclonic shear zones on Jupiter are characterized by chaotic cloud systems, outbursts of bright cloud material and, from recent Galileo results, the occurrence of lightning<sup>16,17</sup>. When the bright cloud's position is corrected for wind advection, it coincides with a NIMS humid area (Fig. 1). Our spectroscopic results of that area greatly strengthen the case that the observed deep clouds are indeed convecting water clouds which result in lightning and the formation of bright cloud materials at higher altitudes. These widespread and energetic convection events may be a dominant source of energy for driving Jupiter's winds<sup>18</sup>. □

Received 8 October 1999; accepted 29 February 2000.

- Weidenschilling, S. J. & Lewis, J. S. Atmospheric and cloud structure of the jovian planets. *Icarus* **20**, 465–476 (1973).
- Atreya, S. K. *et al.* A comparison of the atmospheres of Jupiter and Saturn: deep atmospheric composition, cloud structure, vertical mixing, and origin. *Planet. Space Sci.* **47**, 1243–1262 (1999).

- Drossart, P. & Encenaz, T. The abundance of water on Jupiter from the Voyager IRIS data at 5 microns. *Icarus* **52**, 483–491 (1982).
- Bjoraker, G., Larson, H. P. & Kunde, V. The abundance and distribution of water vapor in Jupiter's atmosphere. *Astrophys. J.* **311**, 1058–1072 (1986).
- Carlson, B. E., Lacinis, A. A. & Rossow, W. B. The abundance and distribution of water vapor in the jovian troposphere as inferred from Voyager IRIS observations. *Astrophys. J.* **388**, 648–668 (1992).
- Niemann, H. B. *et al.* The composition of the jovian atmosphere as determined by the Galileo probe mass spectrometer. *J. Geophys. Res.* **103**, 22831–22845 (1998).
- Regent, B. *et al.* The clouds on Jupiter: results on the Galileo Jupiter mission probe nephelometer experiment. *J. Geophys. Res.* **103**, 22891–22910 (1998).
- Larson, H. P., Fink, U., Treffers, R. & Gautier, T. N. Detection of water vapour on Jupiter. *Astrophys. J.* **197**, L137–L140 (1975).
- Roos-Serote, M. *et al.* Analysis of Jupiter North Equatorial Belt hot spots in the 4–4  $\mu\text{m}$  range from Galileo/near-infrared mapping spectrometer observations: measurements of cloud opacity, water and ammonia. *J. Geophys. Res.* **103**, 23023–23041 (1998).
- Irwin, P. *et al.* Cloud structure and atmospheric composition of Jupiter retrieved from Galileo near-infrared mapping spectrometer real-time spectra. *J. Geophys. Res.* **103**, 23001–23022 (1998).
- Seiff, A. *et al.* Thermal structure of Jupiter's atmosphere near the edge of a 5- $\mu\text{m}$  hotspot in the north equatorial belt. *J. Geophys. Res.* **103**, 22857–22890 (1998).
- Roos-Serote, M., Drossart, P., Encenaz, T., Carlson, R. W. & Leader, F. Constraints on the tropospheric cloud structure of Jupiter from spectroscopy in the 5- $\mu\text{m}$  region: a comparison between voyager/IRIS, Galileo/NIMS, and ISO/SWS spectra. *Icarus* **137**, 315–340 (1999).
- Banfield, D. *et al.* Jupiter's cloud structure from Galileo imaging data. *Icarus* **135**, 230–250 (1998).
- Gierasch, P. *et al.* Cloud structure near convective locations on Jupiter. *Bull. Am. Astron. Soc.* **31**, 115 (1999).
- Limaye, S. S. Jupiter: New estimates of the mean zonal flow at the cloud level. *Icarus* **65**, 335–352 (1986).
- Little, B. *et al.* Galileo images of lightning on Jupiter. *Icarus* **142**, 306–323 (1999).
- Gierasch, P. *et al.* Observation of moist convection in Jupiter's atmosphere. *Nature* **403**, 628–630 (2000).
- Ingersoll, A. P., Gierasch, P. J., Banfield, D. & Vasavada, A. R. Moist convection as an energy source for the large-scale motions in Jupiter's atmosphere. *Nature* **403**, 630–632 (2000).
- Vasavada, A. R. *et al.* Galileo imaging of Jupiter's atmosphere: The Great Red Spot, equatorial region, and white ovals. *Icarus* **135**, 265–275 (1998).

## Acknowledgements

This work was partly carried out at the Jet Propulsion Laboratory, California Institute of Technology, under contract with NASA, through the Jupiter System Data Analysis Program and the Galileo Project. M.R.-S. acknowledges financial support from PRAXIS XXI/FCT (Fundação para a Ciência e a Tecnologia), and the French Embassy/ICCTI (Instituto de Cooperação Científica e Tecnológica Internacional), Portugal. We thank P. Gierasch, D. Banfield and T. Entenaz for very constructive discussions, and J. Yoshimizu for help in making Fig. 1.

Correspondence and requests for materials should be addressed to M. R.-S. (e-mail: roos@oal.ul.pt).

## Closing the spin gap in the Kondo insulator $\text{Ce}_3\text{Bi}_4\text{Pt}_3$ at high magnetic fields

Marcelo Jaime\*, Roman Movshovich\*, Gregory R. Stewart†, Ward P. Beyermann‡, Mariano Gomez Berisso§, Michael F. Hundley\*, Paul C. Canfield|| & John L. Sarrao\*

\*Los Alamos National Laboratory, Los Alamos, New Mexico 87545, USA

†University of Florida, Gainesville, Florida 32611, USA

‡University of California, Riverside, California 92521, USA

§Centro Atómico Bariloche, Bariloche 8400, Argentina

||Ames Laboratory and Department of Physics and Astronomy,

Iowa State University, Ames, Iowa 50011, USA

Kondo insulator materials<sup>1</sup>—such as  $\text{CeRhAs}$ ,  $\text{CeRhSb}$ ,  $\text{YbB}_{12}$ ,  $\text{Ce}_3\text{Bi}_4\text{Pt}_3$  and  $\text{SmB}_6$ —are 3d, 4f and 5f intermetallic compounds that have attracted considerable interest in recent years<sup>2–5</sup>. At high temperatures, they behave like metals. But as temperature is reduced, an energy gap opens in the conduction band at the Fermi energy and the materials become insulating. This contrasts with other f-electron compounds, which are metallic at all

temperatures. The formation of the gap in Kondo insulators has been proposed to be a consequence of hybridization between the conduction band and the *f*-electron levels<sup>6,7</sup>, giving a ‘spin’ gap. If this is indeed the case, metallic behaviour should be recovered when the gap is closed by changing external parameters, such as magnetic field or pressure. Some experimental evidence suggests that the gap can be closed in SmB<sub>6</sub> (refs 5, 8) and YbB<sub>12</sub> (ref. 9). Here we present specific-heat measurements of Ce<sub>3</sub>Bi<sub>4</sub>Pt<sub>3</sub> in d.c. and pulsed magnetic fields up to 60 tesla. Numerical results and the analysis of our data using the Coqblin–Schrieffer model demonstrate unambiguously a field-induced insulator-to-metal transition.

Previous experimental studies have indicated that the spin gap (or ‘Kondo gap’, with a value of  $\Delta$ ) can be closed in SmB<sub>6</sub> with applied pressure<sup>8</sup> and magnetic field<sup>5</sup>, and that the gap in YbB<sub>12</sub> can be closed with an applied magnetic field<sup>9</sup>. (But recent data obtained on CeNiSn, described in the past as a Kondo insulator whose small spin gap can be closed by a moderate magnetic field, have shown this material to have a metallic, rather than insulating, ground state (see ref. 10 and references therein). Attempts have also been made in the past to observe the closure of the gap in Ce<sub>3</sub>Bi<sub>4</sub>Pt<sub>3</sub>; these attempts involved measurements of electrical resistivity<sup>11,12</sup> and magnetization<sup>13</sup>, in both d.c. magnets and in pulsed magnets driven by capacitor banks. While a large negative magnetoresistance was observed in fields up to 60 T at low temperatures and interpreted as an indication of closing of the gap<sup>12</sup>, the magnetization is linear in magnetic field in the same field and temperature ranges.

In the light of these conflicting results, it has been suggested<sup>13</sup> that the recovery of charge carriers observed in the transport properties in magnetic fields might be due to pockets of the Fermi surface where the gap is smaller. Another possibility is that the *g*-factor in Ce<sub>3</sub>Bi<sub>4</sub>Pt<sub>3</sub>, which determines the energy scale of magnetic interactions, is smaller than expected (a larger magnetic field is needed to reach the range  $gJ\mu_B H \approx \Delta$ ) and consequently the observed low-temperature properties are due simply to extrinsic charge carriers<sup>14</sup>. (Here *H* is the magnetic field,  $\mu_B$  is the Bohr magneton and *J* is the electron’s total angular momentum). Measurements of the specific heat in magnetic fields directly probe the evolution of the excitation spectrum, and of the Kondo gap in particular, and can therefore provide the key to understanding the physical origins of the very

distinctive ground-state properties of Kondo insulators, helping in the construction of a complete theoretical model.

The 60-tesla long-pulse (60TLP) magnet, at the National High Magnetic Field Laboratory, Los Alamos Pulsed Field Laboratory, is driven by a 1.4-GW synchronous power generator; this magnet produces a flat-top field for a period of greater than 100 ms at 60 T, and for longer time at lower fields. We have built a calorimeter out of plastic materials that enables us to perform heat-capacity measurements at temperatures between 1.4 and 20 K in this magnet<sup>15</sup>. During the magnetic field pulse, which lasts for about 2 s, the calorimeter can be regarded as thermally isolated, that is, in an adiabatic condition. We used a heat-pulse method, where a known amount of heat is delivered to the calorimeter using a chip resistor, to measure the heat capacity of flux-grown single-crystal samples of Ce<sub>3</sub>Bi<sub>4</sub>Pt<sub>3</sub>. The data collected during a typical experiment on Ce<sub>3</sub>Bi<sub>4</sub>Pt<sub>3</sub> is displayed in Fig. 1, which shows that the calorimeter comes to thermal equilibrium both before and after the heat pulse is delivered within the magnetic field plateau. The temperature is measured during the entire field pulse with a Cernox bare chip resistance thermometer (Lakeshore Inc.), previously calibrated in d.c. field up to 30 T and in pulsed fields up to 60 T. The heat capacity of the sample is determined as the ratio of the heat delivered to the sample to the change in its temperature due to the heat pulse.

The results of the direct measurements of the specific heat *C*(*T*) of a 44.85-mg single-crystal sample of Ce<sub>3</sub>Bi<sub>4</sub>Pt<sub>3</sub> (sample no. 2), performed in magnetic fields up to 60 T, are shown in Fig. 2. *C*(*T*)/*T* is linear in *T*<sup>2</sup>, and the zero-temperature extrapolation  $\gamma_H$  increases from about 18 mJ mol<sup>-1</sup> K<sup>-2</sup> in zero field to close to 60 mJ mol<sup>-1</sup> K<sup>-2</sup> in a field of 60 T. All molar heat capacities reported here are per formula unit. The zero-field Sommerfeld coefficient is slightly larger than the values reported earlier<sup>6</sup> (9–15 mJ mol<sup>-1</sup> K<sup>-2</sup>). This is consistent with measurements of the resistivity ratio in our samples  $\rho(4\text{ K})/\rho(300\text{ K}) \approx 70$ , which is somewhat lower than that previously reported<sup>12</sup>. Both measurements indicate that the present sample contains a slightly larger concentration of defects or impurities. The observed increase in the heat capacity in fields equal to or larger than 30 T is in very good agreement with the reversible temperature change (due to the magnetocaloric effect<sup>15</sup>) observed during the ramp portions of the magnetic field pulse. We note the temperature drop during the ramp-up portion of the field profile in Fig. 1. In order to verify the calibration of our thermometry

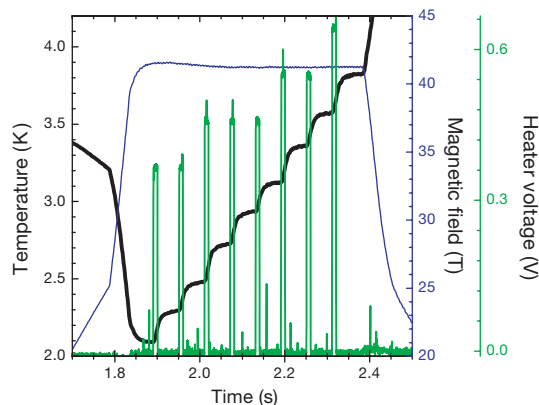


**Figure 1** Heat-capacity experiment in the 60TLP magnet. The magnetic field profile is displayed in blue, the temperature of the Ce<sub>3</sub>Bi<sub>4</sub>Pt<sub>3</sub> (sample no. 1) in black, and eight (10-ms each) heat pulses delivered during the field plateau in green. The temperature decreases during the field ramp-up due to the adiabatic magnetization of the sample, reaches equilibrium before and after each heat pulse is delivered, and increases during the field ramp-down due to the adiabatic demagnetization of the sample.

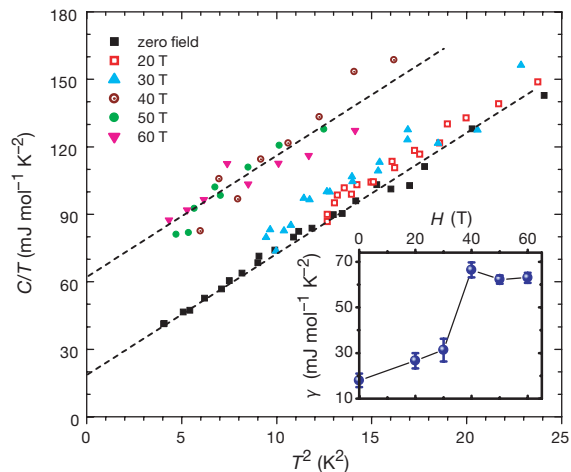


**Figure 2** Specific heat in pulsed fields. Shown is *C*/*T* versus *T*<sup>2</sup> for Ce<sub>3</sub>Bi<sub>4</sub>Pt<sub>3</sub> single-crystal sample no. 2 in magnetic fields between zero and 60 T after subtraction of heat capacity of empty stage. Dashed lines are guides to the eye. Inset shows Sommerfeld coefficient  $\gamma_H = C(H)/T_{T=0}$ ; obtained with a single-parameter fit (field-independent lattice contribution).

and correct operation of the calorimeter, we have also measured the specific heat of a 303-mg Si single crystal, where we do not expect any variation of specific heat with magnetic field. The magnetic field effect observed for this sample is no larger than  $0.1\% T^{-1}$ , in accord with expectation.

In order to tell whether our results indicate the recovery of the metallic Kondo state in high fields, the increase in  $\gamma_H$  observed in  $Ce_3Bi_4Pt_3$  needs to be put in perspective. Magnetic susceptibility<sup>14</sup> and high-temperature neutron quasielastic line width<sup>7,16,17</sup> measurements can be used to estimate a zero-field Kondo temperature of  $T_K^0 = 240\text{--}320$  K. In turn, the Sommerfeld coefficient for a metal with such  $T_K$  can be estimated using the expression for a single-impurity Kondo system<sup>18</sup>:  $\gamma_0 = 3 \times 1.29 \pi R / 6T_K^0 = 53\text{--}70 \text{ mJ mol}^{-1} \text{ K}^{-2}$  (the pre-factor of 3 in the first expression accounts for the number of Ce atoms per formula unit and  $R = 8.31 \text{ J mol}^{-1} \text{ K}^{-1}$  is the gas constant). This provides an upper bound for the high field  $\gamma_H$  in  $Ce_3Bi_4Pt_3$ , as it is expected that an external field will suppress correlations and induce a reduction in  $\gamma_H$ . Taking into account the effect of the applied magnetic fields within a single-impurity model<sup>19</sup>, our estimate of the Sommerfeld coefficient at 60 T is  $\gamma_{60} = 51\text{--}66 \text{ mJ mol}^{-1} \text{ K}^{-2}$ . Hundley *et al.*<sup>6</sup> have measured the compound  $La_3Bi_4Pt_3$  in zero field, and obtained  $\gamma_0 = 27 \text{ mJ mol}^{-1} \text{ K}^{-2}$ . This value in  $La_3Bi_4Pt_3$ , an isostructural metal where electronic correlations are absent, should be our lower bound limit on  $\gamma_{60}$  in the high field metallized state of  $Ce_3Bi_4Pt_3$ .

The inset in Fig. 2 shows  $\gamma_H$  for  $Ce_3Bi_4Pt_3$  sample no. 2, in magnetic fields up to 60 T. The values for  $\gamma_H$  were obtained from a

single-parameter fit of the form  $C(T) = \gamma_H T + \beta_H T^3$  (where  $\gamma_H T$  and  $\beta_H T^3$  are the electronic and phononic contributions in a magnetic field  $H$ , respectively), with the coefficient  $\beta_H$  of the lattice term fixed to its zero-field value. We see a sharp rise in  $\gamma_H$  between 30 and 40 T. The result of the fit suggests a saturation at a value of  $\gamma_H^{\text{sat}} = 62 \pm 3 \text{ mJ mol}^{-1} \text{ K}^{-2}$  above 40 T. The strong enhancement of  $\gamma_H$  from its zero-field value, and the quantitative agreement with the estimate based on  $T_K$  for a metallic ground state of  $Ce_3Bi_4Pt_3$ , prove that we indeed crossed the phase boundary between the Kondo insulator and the Kondo metal.

The bandgap in  $Ce_3Bi_4Pt_3$  should be observable in the temperature dependence of the specific heat at temperatures comparable to the gap, as the conduction band is depopulated. For lower magnetic fields available in d.c. superconducting magnets, we expect the value of the gap to remain high, and therefore, the experimental temperature range must be increased. A thermal relaxation technique was chosen to measure the specific heat of sample no. 2 in a superconducting magnet at temperatures between 4 and 60 K (ref. 20). The results of this experiment,  $C/T$  versus  $T$ , in zero field and 18 T, are displayed in Fig. 3a. We have subtracted the zero-field specific heat ( $C_0$ ) from the specific heat in 18 T ( $C_{18}$ ) to remove the non-field-dependent components, such as the phonon contribution, and divided the difference by the temperature. In this way we obtain the differential Sommerfeld coefficient at 18 T  $\Delta\gamma_{18}(T)$  and display it in the inset of Fig. 3a.  $\Delta\gamma_{18}$  is rapidly suppressed below 30 K, and remains finite at lower temperatures. This suggests a change in the magnitude of the gap, and a concomitant loss of charge carriers as the temperature is reduced. The error due to magnetoresistance in our temperature sensor (1% in  $T$  and 0.5% in  $C_{18}$  below 20 K) has been taken into account. The scatter (0.3% of  $C_0, C_{18}$ ) reflects the typical reproducibility error of the experiment, and results in a relatively large error bar for the residual value  $\Delta\gamma_{18|T \rightarrow 0} = 13 \pm 7 \text{ mJ mol}^{-1} \text{ K}^{-2}$ .

We calculated the specific heat of a system with the following properties: narrow valence and conduction bands of equal width  $BW$  ( $= 600$  K), separated by a gap  $\Delta$ , and a narrower impurity band of width  $w$  ( $= 100$  K) centred at the chemical potential  $\mu$ , which is suggested theoretically<sup>21</sup> as an explanation for the observed finite  $\gamma_0$  (see Fig. 3a). In this model it was assumed that each band can accommodate  $2N$  electrons, where  $N$  is the number of Ce atoms in the sample. We performed the computation for two cases: a fully open gap, and a reduced gap. The band widths remain constant, and the central band weight increases, when the gap is reduced. The spectral weight of the central band was chosen to reproduce the experimental  $\gamma_0$  when the gap is open, and it is able to accommodate 0.96% of the total number of states in one band. Similar models (without the states in the gap) were used previously to simulate the zero-field electronic specific heat<sup>22,23</sup> of  $Yb_xLu_{1-x}B_{12}$  and  $SmB_6$ , and the NMR spin–lattice relaxation rate<sup>24</sup> of  $Ce_3Bi_4Pt_3$ . The difference between calculated specific heat in each case (with  $\Delta = 155$  K and  $\Delta = 220$  K, simulating 18 T and zero field, respectively) is the solid line in the inset of Fig. 3a. The quantitative agreement with the data is evident.

The difference  $\Delta C$  can remain finite at low temperatures only if some increase of the density of states at the chemical potential is allowed when the gap is reduced. The number of states we use for 18 T simulation is 1.7% of the states in the valence band. For comparison, a calculation with identical parameters and fixed (field independent) density of states at  $\mu$  is the dashed line in the inset of Fig. 3a. The small but steady increase in  $\gamma_H$  observed in the pulsed-field experiment below 30 T (Fig. 2) and the finite  $\Delta\gamma_{18|T \rightarrow 0}$  (inset in Fig. 3a) indicate that the effect of the applied field is to reduce the gap (Fig. 3b) as well as to increase the density of states inside the gap. The value obtained in our fit for the zero-field gap is in excellent agreement with the spin gap  $\Delta_s = 250$  K observed in optical experiments<sup>25</sup>. The gap value that we use to fit the specific-heat results is larger than the gap observed in transport experiments.

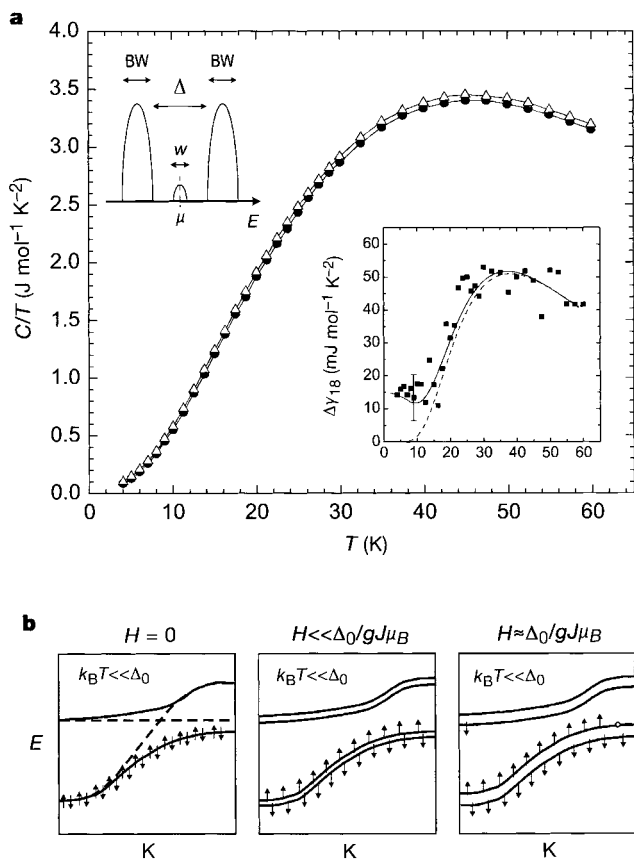


**Figure 3** Specific heat measured in d.c. fields. **a**,  $C/T$  versus temperature  $T$  in zero field (solid circles) and 18 T (triangles), and diagram for the ‘two narrow bands’ model described in the text. Inset shows the differential Sommerfeld coefficient in a field of 18 T,  $\Delta\gamma_{18} (= [C_{18} - C_0]/T)$ , versus  $T$ . The lines are fits with the ‘two narrow bands’ model, with field-dependent (solid line) and field-independent (dashed line) impurity band at the chemical potential. **b**, Schematic band structure and magnetic field dependence in a Kondo insulator at low temperatures. Modified from ref. 1.

This discrepancy can be reconciled if one takes into account the impurity band centred at the chemical potential. Indeed, if the states in this band are localized or have small mobility at low temperatures, the conductivity of the material is very poor, as observed<sup>11</sup>. As the temperature is increased, the relevant energy scale is the difference between the top of the impurity band and the bottom of the conduction band, which is 60 K in our fit and in very good agreement with the transport experiments<sup>11,12</sup>. The reduction of the band gap observed in a field of 18 T is consistent with our low-temperature results that show the gap closing above 30 T. We also see that the magnitude of  $\Delta\gamma_{18}$  at temperatures above 30 K, where the 18 T gap is expected to be effectively closed and the zero field gap to be open, is  $50 \pm 5 \text{ mJ mol}^{-1} \text{ K}^{-2}$ , in good agreement with the saturation value  $\gamma_H^{\text{sat}}$  for magnetic fields above 40 T at low temperatures.

These results of thermodynamic measurements add information to what we know about Kondo insulators from transport measurements in high fields<sup>5,9,12</sup>, and should aid in the construction of a theoretical model for this class of strongly correlated compounds. Additionally, in the course of these studies, we have demonstrated the feasibility of direct specific-heat measurements in the extreme conditions of the pulsed magnetic fields produced by the 60TLP magnet at the National High Magnetic Field Laboratory. □

Received 27 October 1999; accepted 14 March 2000.

1. Aeppli, G. & Fisk, Z. Kondo insulators. *Comments Cond. Mat. Phys.* **16**, 155–165 (1992).
2. Kumigashira, H. *et al.* Spectral evidence for pseudogap formation in Kondo insulators CeRhAs and CeRhSb. *Phys. Rev. Lett.* **82**, 1943–1946 (1999).
3. Susaki, T. *et al.* Temperature-dependent high-resolution photoemission study of the Kondo insulator YbB<sub>12</sub>. *Phys. Rev. Lett.* **82**, 992–995 (1999).
4. Breuer, K. *et al.* Photoemission-study of the Kondo insulator Ce<sub>3</sub>Bi<sub>4</sub>Pt<sub>3</sub>. *Europhys. Lett.* **41**, 565–570 (1998).
5. Cooley, J. C. *et al.* High field gap closure in the Kondo insulator SmB<sub>6</sub>. *J. Supercond.* **12**, 171–173 (1999).
6. Hundley, M. F. *et al.* Hybridization gap in Ce<sub>3</sub>Bi<sub>4</sub>Pt<sub>3</sub>. *Phys. Rev. B* **42**, 6842–6845 (1990).
7. Thompson, J. D. in *Transport and Thermal Properties of f-Electron Systems* (eds Fujii, H., Fujita, T. & Oomi, G.) 35–48 (Plenum, New York, 1993).
8. Moshchalkov, V. V. *et al.* SmB<sub>6</sub> at high-pressures: the transition from insulating to the metallic Kondo lattice. *J. Magn. Magn. Mat.* **47&48**, 289–291 (1985).
9. Sugiyama, K. *et al.* Field-induced metallic state in YbB<sub>12</sub> under high magnetic-field. *J. Phys. Soc. Jpn* **57**, 3946–3953 (1988).
10. Izawa, K. *et al.* Metallic ground state of CeNiSn. *Phys. Rev. B* **59**, 2599–2603 (1999).
11. Hundley, M. F. *et al.* Magnetoresistance of the Kondo insulator Ce<sub>3</sub>Bi<sub>4</sub>Pt<sub>3</sub>. *Physica B* **186–188**, 425–427 (1993).
12. Boebinger, G. S., Passner, A., Canfield, P. C. & Fisk, Z. Studies of the Kondo insulator Ce<sub>3</sub>Bi<sub>4</sub>Pt<sub>3</sub> in 61-T pulsed magnetic-fields. *Physica B* **211**, 227–229 (1995).
13. Modler, R. in *Physical Phenomena at High Magnetic Fields-III* (eds Fisk, Z., Gor'kov, L. & Schrieffer, R.) 154–159 (World Scientific, Singapore, 1999).
14. Hundley, M. F. *et al.* Evidence for a coherence gap in Ce<sub>3</sub>Bi<sub>4</sub>Pt<sub>3</sub>. *Physica B* **171**, 254–257 (1991).
15. Jaime, M. *et al.* in *Physical Phenomena at High Magnetic Fields-III* (eds Fisk, Z., Gor'kov, L. & Schrieffer, R.) 148–153 (World Scientific, Singapore, 1999).
16. Severing, A. *et al.* Gap in the magnetic excitation spectrum of Ce<sub>3</sub>Bi<sub>4</sub>Pt<sub>3</sub>. *Phys. Rev. B* **44**, 6832–6837 (1991).
17. Hewson, A. C. *The Kondo Problem to Heavy Fermions* (Cambridge Univ. Press, Cambridge, 1993).
18. Rajan, V. T. Magnetic-susceptibility and specific-heat of the Coqblin-Schrieffer model. *Phys. Rev. Lett.* **51**, 308–311 (1983).
19. Schotte, K. D. & Schotte, U. Interpretation of Kondo experiments in a magnetic-field. *Phys. Lett. A* **55**, 38–40 (1975).
20. Bachmann, R. *et al.* Heat capacity measurements on small samples at low temperatures. *Rev. Sci. Instrum.* **43**, 205–214 (1972).
21. Schlottmann, P. Impurity bands in Kondo insulators. *Phys. Rev. B* **46**, 998–1004 (1992).
22. Iga, F., Kasaya, M. & Kasuya, T. Specific-heat measurements of YbB<sub>12</sub> and Yb<sub>2</sub>Lu<sub>1-x</sub>B<sub>12</sub>. *J. Magn. Magn. Mat.* **76&77**, 156–158 (1988).
23. Mandrus, D. *et al.* Low-temperature thermal-expansion of SmB<sub>6</sub>: evidence for a single-energy scale in the thermodynamics of Kondo insulators. *Phys. Rev. B* **49**, 16809–16812 (1994).
24. Reyes, A. P. *et al.* Bi-209 NMR and NQR investigation of the small-gap semiconductor Ce<sub>3</sub>Bi<sub>4</sub>Pt<sub>3</sub>. *Phys. Rev. B* **49**, 16321–16330 (1994).
25. Degiorgi, L. The electrodynamic response of heavy-electron compounds. *Rev. Mod. Phys.* **71**, 687–734 (1999).

**Acknowledgements**

We thank Z. Fisk, J. D. Thompson and P. Schlottmann for discussions; J. Kim for his assistance with the thermometry calibration in the 30 T d.c. magnet at the NHMFL/Tallahassee; and D. Rickel, C. Mielke, J. Betts, J. Schillig, J. Sims and M. Pacheco for technical assistance and operation of the 60TLP magnet.

Correspondence and requests for materials should be addressed to M.J. (e-mail: mjaime@lanl.gov)

**Relaxation in polymer electrolytes on the nanosecond timescale**

Guomin Mao\*, Ricardo Fernandez Perea\*, W. Spencer Howells†, David L. Price\* & Marie-Louise Saboungi\*

\* Argonne National Laboratory, Argonne, Illinois 60439, USA

† Rutherford-Appleton Laboratory, Chilton, Oxfordshire OX11 0QX, UK

The relation between mechanical and electrical relaxation in polymer/lithium-salt complexes is a fascinating and still unresolved problem in condensed-matter physics<sup>1</sup>, yet has an important bearing on the viability of such materials for use as electrolytes in lithium batteries. At room temperature, these materials are biphasic: they consist of both fluid amorphous regions and salt-enriched crystalline regions. Ionic conduction is known to occur predominantly in the amorphous fluid regions. Although the conduction mechanisms are not yet fully understood<sup>2</sup>, it is widely accepted that lithium ions, coordinated with groups of ether oxygen atoms on single or perhaps double polymer chains, move through re-coordination with other oxygen-bearing groups<sup>3,4</sup>. The formation and disruption of these coordination bonds must be accompanied by strong relaxation of the local chain structure. Here we probe the relaxation on a nanosecond timescale using quasielastic neutron scattering, and we show that at least two processes are involved: a slow process with a translational character and one or two fast processes with a rotational character. Whereas the former reflects the slowing-down of the translational relaxation commonly observed in polyethylene oxide and other polymer melts, the latter appears to be unique to the polymer electrolytes and has not (to our knowledge) been observed before. A clear picture emerges of the lithium cations forming crosslinks between chain segments and thereby profoundly altering the dynamics of the polymer network.

The close relationship between ion transport and polymer relaxation has stimulated a considerable body of work on the dynamics of these systems. In particular, NMR line shapes and spin-lattice relaxation rates provide an effective probe of these dynamics on the microsecond to second timescale. For polymer electrolytes made of polyethylene oxide (PEO) with a number of

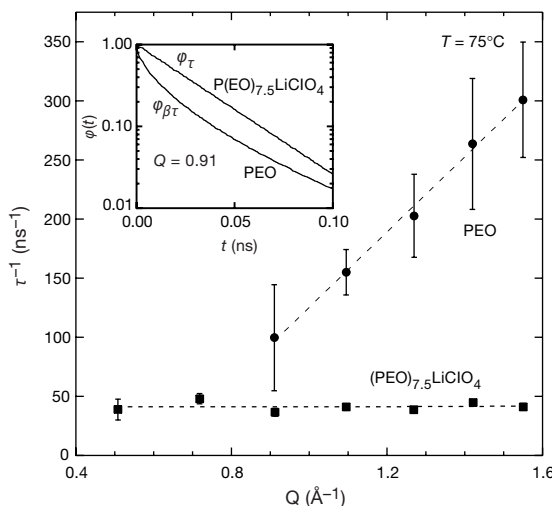


**Figure 1** Variations of the inverse relaxation times  $\tau^{-1}$  for pure PEO and P(EO)<sub>7.5</sub>LiClO<sub>4</sub> electrolyte at 75°C. Inset, behaviour of  $\phi_{\beta\tau}(t)$  and  $\phi_{\tau}(t)$  for the two systems at  $Q = 0.91 \text{ \AA}^{-1}$ . Dashed lines are guides for the eye.